Journal of Zhejiang University-SCIENCE B (Biomedicine & Biotechnology) *2022 23(7):564-577*
www.jzus.zju.edu.cn; www.springer.com/journal/11585
E-mail: jzus_b@zju.edu.cn

Research Article
https://doi.org/10.1631/jzus.B2100701

High-throughput "read-on-ski" automated imaging and label-free detection system for toxicity screening of compounds using personalised human kidney organoids

Qizheng WANG[1], Jun LU[2,3], Ke FAN[2], Yiwei XU[2], Yucui XIONG[2], Zhiyong SUN[2,3], Man ZHAI[2], Zhizhong ZHANG[2,3], Sheng ZHANG[2], Yan SONG[2], Jianzhong LUO[2], Mingliang YOU[4], Meijin GUO[1]✉, Xiao ZHANG[2,3]✉

[1]*State Key Laboratory of Bioreactor Engineering, East China University of Science and Technology, Shanghai 200237, China*
[2]*Guangzhou Institutes of Biomedicine and Health, Chinese Academy of Sciences, Guangzhou 510530, China*
[3]*Bioland Laboratory (Guangzhou Regenerative Medicine and Health Guangdong Laboratory), Guangzhou 510320, China*
[4]*Hangzhou Cancer Institute, Key Laboratory of Clinical Cancer Pharmacology and Toxicology Research of Zhejiang Province, Affiliated Hangzhou Cancer Hospital, Zhejiang University School of Medicine, Hangzhou 310002, China*

Abstract: Organoid models are used to study kidney physiology, such as the assessment of nephrotoxicity and underlying disease processes. Personalized human pluripotent stem cell-derived kidney organoids are ideal models for compound toxicity studies, but there is a need to accelerate basic and translational research in the field. Here, we developed an automated continuous imaging setup with the "read-on-ski" law of control to maximize temporal resolution with minimum culture plate vibration. High-accuracy performance was achieved: organoid screening and imaging were performed at a spatial resolution of 1.1 μm for the entire multi-well plate under 3 min. We used the in-house developed multi-well spinning device and cisplatin-induced nephrotoxicity model to evaluate the toxicity in kidney organoids using this system. The acquired images were processed via machine learning-based classification and segmentation algorithms, and the toxicity in kidney organoids was determined with 95% accuracy. The results obtained by the automated "read-on-ski" imaging device, combined with label-free and non-invasive algorithms for detection, were verified using conventional biological procedures. Taking advantage of the close-to-in vivo-kidney organoid model, this new development opens the door for further application of scaled-up screening using organoids in basic research and drug discovery.

Key words: Kidney organoid; High-throughput microscopy; Nephrotoxicity; Machine learning

1 Introduction

The mammalian kidney is crucial for filtering blood and maintaining the osmolarity of body fluids. Kidney disorders caused by both acute and chronic injuries affect over 10% of the human population worldwide (Imig and Ryan, 2013). Renal disease is attributed to various causes, including genetics, injuries, and medication. Kidney problems can develop suddenly (acute kidney injury, a sudden episode of kidney failure, or kidney damage within a few hours or days) or over a long period (chronic kidney disease, low detection rate). Annually, about 2.2 million people with end-stage kidney disease die prematurely, unable to access treatment (Liyanage et al., 2015). To date, no single type of renal cell can fulfil the requirements for application in assessing compound efficacy or safety screening, and research in regenerative medicine for bioartificial kidneys or disease modelling has been limited. In recent years, significant progress has been made towards overcoming this important hurdle, and in vitro derived functional human renal cells and mini tissues have been developed (Tasnim et al., 2010; Jansen et al., 2014; Tiong et al., 2014). The differentiation of induced pluripotent stem cells (iPSCs) and

✉ Xiao ZHANG, zhang_xiao@gibh.ac.cn
Meijin GUO, guo_mj@ecust.edu.cn
Xiao ZHANG, https://orcid.org/0000-0002-3894-8513
Meijin GUO, https://orcid.org/0000-0002-3171-4802

Received Aug. 7, 2021; Revision accepted Feb. 4, 2022;
Crosschecked June 27, 2022

their plasticity in response to developmental signals (Carpenter et al., 2009; Ichimura and Shiba, 2017) make them a promising and logical choice for modelling monogenic diseases and compound screening (Ebert et al., 2009; Shi et al., 2017). Furthermore, iPSC-derived progenitor cells can be differentiated and self-organized to form complex three-dimensional (3D) spheroids with a structured multicell-type arrangement in vitro. These organoids serve as mini tissues with specific structures and functions to mimic in vivo organs. Hence, 3D kidney organoids in suspension cultures are ideal models to study renal disease in vitro, and serve as a more advanced multicellular system to substitute two-dimensional (2D) adherent cells currently used in high-throughput compound library screening.

As mini-tissue-like kidney organoids are generated in 3D suspension cultures (Tasnim et al., 2010; Ciampi et al., 2016), the mini tissues resemble certain kidney structures and contain various cell types and patterns similar to those present in vivo. Although kidney organoids have not shown full renal function, a differentiated multicellular arrangement containing the structure of nephrons and GATA-binding factor 3 (GATA3)-positive tubule formation has been reported (Davies, 2015). Several studies have shown that kidney organoids can be applied in renal disease or injury modelling as well as in nephrotoxicity screening. In a recent study, brain organoids were cultured in a miniaturized spinning bioreactor unit, which can reduce the culturing volume by 50-fold under 12–24 different conditions (Qian et al., 2016). Hence, we previously developed a mini-spin renal organoid culturing device in multi-well batches to enhance the throughput of compound screening, which is known as “mini renal tissues in a dish” (Fig. S1). However, there is still a strong need to investigate compound toxicity in a label-free non-invasive manner.

Monitoring cellular morphology changes is the conventional approach for imaging-based living cell assays, which are essential in compound toxicology studies (Su et al., 2016). Light microscopy for continuous imaging of living samples shows great potential to explain cellular response dynamics compared to the microscopy of fixed samples as the endpoint assay. The optical system for imaging living cells needs to consider three aspects: quality of detection, speed of acquisition, and viability of the specimen (Stephens and Allan, 2003). Living cell image quality and acquisition involve a trade-off between spatial and temporal resolution, as the duration of imaging outside the culturing environment needs to be as short as possible (Jones et al., 2011). Unlike 3D tumour spheroids, renal organoids cannot be derived from a single cell in a static state at the bottom of the plate; the embryo body-derived renal organoids in suspension are required to avoid any vibrations during acquisition. Moreover, renal organoids contain structured multicellular arrangements as a result of nephrogenesis; hence, monitoring cellular morphological changes in a label-free and non-invasive manner is a technical requirement for tubule and structure detection in 3D organoids used as a compound screening toxicology model.

The transmitted bright-field imaging approach is the conventional and classic method for label-free and non-invasive multicellular structure detection (Fan et al., 2017). Traditionally, it contains only limited information that can be quantified; however, computer vision can consistently extract the feature information required to quantify a structured multicellular arrangement automatically. This computer-vision-driven approach requires high-quality image input for accurate detection and feature recognition. As the conventional setup, the optical stage performs multiple cycles of “stop-read” control for maximizing the coverage of the well-plate to capture the screening events. To coordinate the movement and the focusing period, this “stop-read” mode causes a reduction in the time resolution for exchanging spatial information. Living cellular imaging is not ideal for a prolonged period outside the incubation environment (Hinchcliffe, 2005). In a commercial setup, the use of an automated optical stage as a continuous imaging approach can increase the imaging speed (Wijnen et al., 2016). However, zigzag motion causes noticeable vibration in suspension spheroids and an inevitable shadow that impairs feature detection efficiency (Sirenko et al., 2015). Hence, label-free imaging detection for organoids requires a system that provides high speed in conjunction with high spatial resolution and limited system vibration.

The renal organoid model is the most relevant and easy to mimic in vivo model (Koning et al., 2020). Combined with a suitable imaging system and detection method, it is an ideal tool for cellular mechanism studies and compound screening. In this study, we report the development of a continuous renal organoid

imaging and screening detection system, called "read-on-ski," which is suitable for automated feature detection in continuous batches. This imaging system integrates a fixed sample stage with an autofocusing strategy and is suitable for downstream image processing in a machine learning approach, which potentially fulfils the requirements of automated 3D organoid structure detection under various conditions. Using a laboratory-made multi-well spinning device for renal organoid batch culturing combined with our in-house developed "read-on-ski" technology, we can perform organoid imaging with 1.1-μm resolution for the entire multi-well plate under 3 min and achieve 95% accuracy in conjunction with the label-free detection algorithm. This system allows us to perform renal organoid-based compound screening in batches using a fully automated approach.

2 Materials and methods

2.1 "Read-on-ski" imaging system

We developed a "read-on-ski" imaging solution for screening organoids cultured in suspension medium. The method uses the latest hardware and software technology and a novel control mechanism with an autofocus technique that fulfils the requirements for high-speed and sub-micron resolution (Fig. 1).

The instrument was equipped with a 5.5-megapixel high-speed camera (Andor Zyla 5.5 scientific Complementary Metal-Oxide-Semiconductor (sCMOS), 100 frame images per second) connected via camera link 10, which matches the speed of our in-house developed optical stage. The hardware allows the image acquisition time to be optimized via a control mechanism. The motion control hardware to operate the multi-axis synchronization of the multi-coordinate system was implemented via the Advanced RISC Machine (ARM)+Digital Signal Processing (DSP)+Field Programmable Gate Array (FPGA) multi-core setup, which was developed in-house as described previously (Lu et al., 2022). The duration of the image acquisition process can be reduced by increasing the speed of the optical stage, which matches the camera frame rate. This non-stop ski-like motion was named "read-on-ski," rather than the conventional "stop-and-read." The only stops for the "read-on-ski" motion are at the edge of the multi-well plate to perform tuning for the second row of the image acquisition. The system uses Köhler illumination alignment with high-dose flash illumination to increase the uniformity of illumination and sampling speed. The illumination scheme needs to deliver a brighter flash continuously, without additional charging, in the shortest period to match the speed required. Therefore, we developed a light source equipped with a Cree XR-E high-power light-emitting diode (LED), combined with a control board and power pack. These can generate flashes as short as 1 μs in duration when the illumination source is triggered. In addition, to create enough photons for sufficient exposure, LED brightness can be increased by altering the current instead of the voltage, for a short pulse.

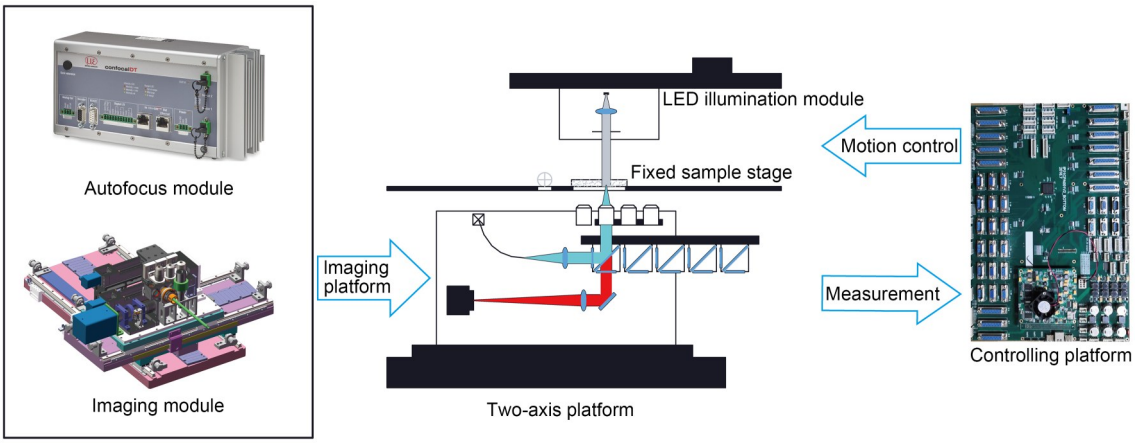

Fig. 1 Design of the "read-on-ski" system. A bright field microscope is integrated on a two-axis platform with an autofocus module. The imaging process is controlled by an in-house developed control board. The autofocus signal is processed by the onboard FPGA chip in real time. FPGA: Field Programmable Gate Array; LED: light-emitting diode.

2.2 Controlling the "read-on-ski" system

The exposure time, flash time, stage movement, and camera acquisition time need to be precisely controlled and managed to capture sufficient light to penetrate the organoid samples at high speed and submicron resolution. For example, a trans-illumination light source is crucial for allowing the light to pass through the organoids to obtain a structuralized pattern image. However, specification of the flash frequency combined with light is also equally essential to achieve fast motion with blur-free images and an adequate signal-to-noise ratio under "read-on-ski." The pulse shape can be tuned according to the exposure time, as required. Unlike monolayer or suspension cell imaging, organoids allow less light to pass through. Hence, the image acquisition time needs to be adapted to serve the needs of feature detection. All components were controlled by a C++ program developed in-house, such that during imaging the stage moves continuously, but the multi-well plate is static. The control method is based on a quantic polynomial S-curve acceleration and deceleration motion control algorithm and a multi-coordinate/multi-axis synchronous interpolation motion control algorithm. This facilitates continuous imaging and limits motion blur (Fig. 2).

2.3 Autofocusing of "read-on-ski" imaging

The bottom of a multi-well plate is an uneven concave surface (Fig. S2). The focus distance is variable during the entire imaging process. Hence, the conventional software autofocus approach does not work robustly with a significant deviation of the focal plane, as in the case of multi-well plates (a few hundred microns). In continuous motion, the focusing distance changes significantly, and the time for focus distance measurement and lens *Z*-axis adjustment is limited. A focus map is required for the motion-control system. We have combined a conventional software-based method and a hardware-based confocal chromatic measurement device to build a focus map in our system. A 5×5 Sobel operator-based contrast-detection autofocus algorithm is implemented to guide the lens for *Z*-axis movement to determine the best focus distance in the well. The upper plate bottom where the cell culture medium was attached was detected using a confocal chromatic distance measurement system (confocal DT 2451, MICRO-EPSILON, Ortenburg, Germany). The device was used while scanning the entire plate in a meander-like motion to collect the data. The captured 3D point cloud data (x, y, and depth) were fitted to a quadric surface to filter noise and approximate offset. The focus map at each image point can be calculated from the original focal plane detected using an image contrast processing method to generate the point correction with the offsets. With this information, it is possible to calculate the absolute geometrical position of the upper plate bottom and hence the focal plane where the organoids are located during drug screening.

2.4 Image stitching and calibration

During continuous motion, it is difficult to capture the gap between each image perfectly with equal distance because the motor and control will contribute to delay and noise. To correct the offset, the images should have a 5% overlap between each other. Adjacent images are aligned based on the Fourier shift theorem (Bracewell, 1986) (Fig. 3).

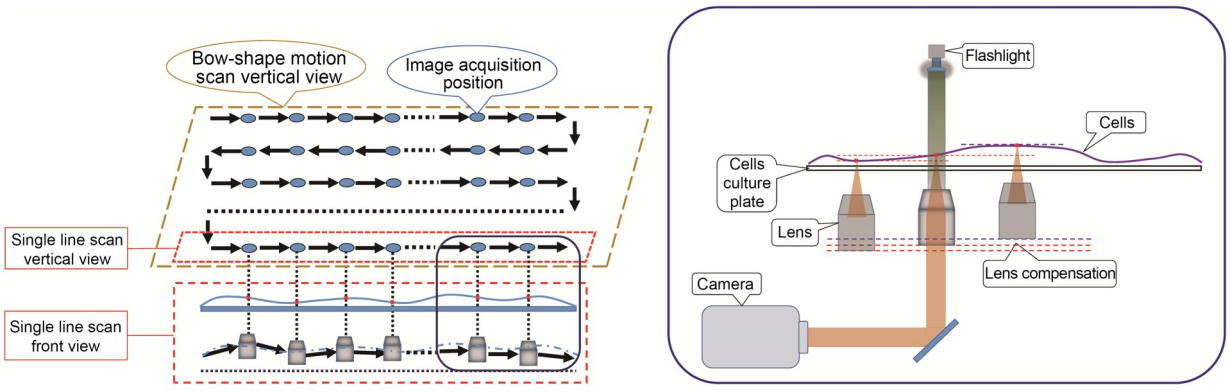

Fig. 2 Schematic diagram of the continuous scanning and autofocus system.

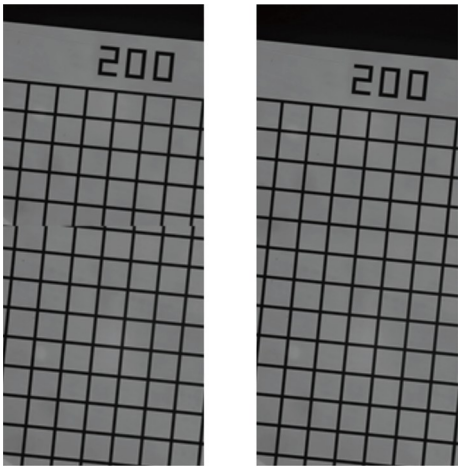

Fig. 3 Comparison between direct stitching (left) and aligning (right). The aligning process can significantly reduce bias in the image.

The size of the image is related to the magnification of the lens and the size of the individual pixels. The mean aligned offset indicates the difference between the actual image edge length and motion step size. To measure the difference between the image and the motion steps precisely, we applied stitching-based calibration. In this case, we used the ideal size as the step distance to image a line grid glass slide (each grid is 200 μm×200 μm). The mean offset after alignment shows that the actual size is 7 μm (vertical)× 10 μm (horizontal), which is larger than the theoretical size in the case of a 10× lens.

2.5 Computer-assisted organoid imaging system

After the screening of the entire culture plate, examination of the morphology of the organoids indicates their developmental status. Therefore, we adopted a procedure that includes the detection and recognition stage, which was developed in our previous study (Fan et al., 2017). Our strategy was to segment out the candidate organoids and then automatically classify them into one of three classes (positive, negative, or adhesion). The organoids, with their thickness and biomass, show lower illumination intensity than the background. Because of this peculiarity, intensity threshold-based binarization typically shows limited grouping capacity. Here, a simplified U-net model (Ronneberger et al., 2015) was applied to separate the organoids from the background. Subsequently, all connected components in the binary images were labelled and cropped out as organoid images. To enhance the contrast, we used the Contrast Limited Adaptive Histogram Equalization (CLAHE) algorithm for each organoid image before classification (Zuiderveld, 1994). After size normalization, all organoids were recognized by a shrunken AlexNet (Krizhevsky et al., 2012), which has only 118 862 parameters, which is less than 0.2% of the original 6×10^7 parameters. To enrich the training set, rotating and flipping were applied to each labelled training image. Consequently, the training set had 28 128 processed images, although we labelled only 1758 images. The training set was not perfectly balanced. Adhesion samples accounted for only 15% of the total samples. Weights for adhesion, positive, and negative samples were set to 0.8, 0.1, and 0.1, respectively, to rebalance the results. The system returned the position and label for each organoid based on the detection and recognition procedure (Fig. S3). The overall accuracy of the entire system was greater than 95%. The positive, negative, and adhesion images recognized by the machine were evaluated by three experienced researchers and further characterized using standard biological experimental verification. The correct images were selected and counted, and the accuracy rate was calculated as the average of the confirmed positive, negative, and adhesion rates of individual experiments.

2.6 Organoid culturing and compound treatment

The human iPSCs used in this study were produced from urine-derived cells from healthy donors following a previously described protocol (Sun et al., 2020). The culturing of iPSC-derived kidney organoids in this study was initiated according to the method proposed by Przepiorski et al. (2018) and performed as previously described (Wang et al., 2021). Kidney organoid generation was conducted as a two-step protocol. First, iPSCs were cultured on 10-cm Matrigel-coated dishes to approximately 80% confluence, then dissociated with dispase, scraped, and resuspended in bovine serum albumin polyvinylalcohol essential lipid (BPEL) medium containing 8 μmol/L CHIR99021, 3.3 μmol/L Y27632, and 1 mmol/L β-mercaptoethanol, and evenly distributed into six-well ultra-low attachment plates (Corning, New York, USA). Half medium changes were carried out using BPEL supplemented with 8 μmol/L CHIR99021 on Day 2. The formed embryoid bodies were transferred into Stage II medium on Day 3 and grown for various periods until kidney

organoids formed (up to two weeks); half of the medium was replaced every 2 d during organoid culturing. The compound treatment was initiated using cisplatin (Sigma-Aldrich, St. Louis, USA), which was considered as the test model for the toxicity study. The treatment was modified as described by Digby et al. (2020). Cisplatin was added at different concentrations (0, 50, or 100 μmol/L) to the Stage II medium of each well on Day 10, and organoids were harvested for downstream analysis after 96 h of treatment.

For drug screening in 96-well plates, well-developed organoids on Day 10 were transferred to 96-well ultra-low attachment plates (Corning), with a single organoid per well, for each compound treatment. Different concentrations of cisplatin, celastrol (Sigma-Aldrich), and vitamin C (Sigma-Aldrich) were used for the panel assay. Cisplatin was administered at 0.5, 50, or 100 μmol/L, celastrol at 5 or 10 μmol/L, and vitamin C at 50 or 200 μmol/L. Organoids cultured with the complete medium were set as the control group. A continuous time-lapse imaging approach was performed using the "read-on-ski" system for each group every 24 h until the treatment reached the end of the 96-h duration.

2.7 Biological analysis

Haematoxylin and eosin (H&E) staining was performed according to standard procedures. Immunocytochemical and reverse transcription-quantitative polymerase chain reaction (RT-qPCR) analyses were performed as previously described (Wang et al., 2021). The antibodies and dyes used in the study included cadherin-1 (CDH1; BD Biosciences, Franklin Lakes, USA), megalin/lipoprotein receptor-related protein-2 (LRP2) (Abcam, Cambridge, UK), kidney injury molecule-1 (KIM1; R&D Systems, Minneapolis, USA), and lotus tetragonolobus lectin (LTL; Vector Labs, Newark, USA). 4',6-Diamidino-2-phenylindole (DAPI; Thermo Fisher Scientific, Waltham, USA) was used for nuclear staining. Immunofluorescence was visualized using a Zeiss LSM710 confocal microscope (Oberkochen, Germany). Organoids were homogenized in TRIzol (Invitrogen, Carlsbad, USA). Total RNA was extracted using the RNeasy Mini Kit (Qiagen, Hilden, Germany), and complementary DNA (cDNA) was synthesized using the GoScript Reverse Transcription system (Promega, Madison, USA). For RT-qPCR, SsoAdvanced SYBR Green Supermix (Bio-Rad, Irvine, USA) was used on an ABI StepOnePlus real-time PCR machine (Applied Biosystems, Foster City, USA). The expression level of each gene was normalized to the glyceraldehyde-3-phosphate dehydrogenase (GAPDH) expression level. Gene expression values were calculated using the $\Delta\Delta C_T$ method. The primer sequences included the following: KIM1, forward 5'-TGTCTGGACCAATGGAACCC-3', reverse 5'-GGCAACAATATACGCCACTGT-3'; tumor necrosis factor-α (TNF-α), forward 5'-GAGGCCAAGCCCTGGTATG-3', reverse 5'-CGGGCCGATTGATCTCAGC-3'; GAPDH, forward 5'-TGCACCACCAACTGCTTAGC-3', reverse 5'-GGCATGGACTGTGGTCATGAG-3'.

2.8 Multiple logistic regression analysis

Multiple logistic regression (Hosmer and Lemesbow, 1980) was applied to illustrate the contributions of both cisplatin concentrations and area changes in response to cisplatin treatment. In the regression model design, cisplatin concentration was considered a predictor variable with four discrete values: 0 representing the control group, and 0.5, 50, and 100 representing the groups treated with 0.5, 50, and 100 μmol/L cisplatin, respectively. Delta area, which is another independent predictor variable, was defined as the change in the area after cisplatin treatment. As for the response variable, a binary variable was adopted due to the binary nature of the final status (organoids in the positive or negative category) of the experiment: 0 for positive outcomes or 1 for negative outcomes (Fig. S4).

3 Results

3.1 System performance of "read-on-ski"

Experiments were performed to validate the performance of the "read-on-ski" microscopy system in terms of resolution and scanning speed. In the resolution view, our system has three different resolution setups, 0.31, 0.62, and 1.55 μm/pixel. This gives us the flexibility to choose between time consumption and resolution to fit different requirements. Utilizing the "read-on-ski" motion, a 40× objective can achieve a speed of 0.62 cm^2/min for the entire microplate. The image duration can be reduced by approximately 14%, 4%, and 3% when 4×, 10×, and 20× objectives are used, respectively, compared to that by the

conventional "stop-and-read" system; data were presented at the same setup as the two commercial control mechanisms (Table 1). The scanning speed is more than twice as fast (for conventional resolution setup) as that of commercial systems (Table 1). Controlling the speed of the stage movement is key to managing vibration and blurring in the image for high-throughput performance, which is also constrained by the speed of the camera (frames per second) and the computation-based image processing. To this end, the "read-on-ski" system was used to examine the resolution over different stage movements. Measurements of resolution were taken from the same region of a standard-resolution board. The integration time and illustration intensity were fixed at 0.01 s and 2.59 mW/mm^2 to accommodate the highest recording speed of the camera. To meet the requirement of organoid screening, a 10× lens was selected for the image acquisition speed test. The example image in Fig. 4 shows that from 2 to 30 mm/s, the speed increase did not significantly affect the resolution. Therefore, we chose 15 mm/s as a stable and sufficiently fast speed for our application. However, the highest running speed is theoretically limited to less than 70 mm/s by the camera's frame rate. Whole-well scanning of a six-well plate was performed using two different lens resolution setups to evaluate the speed of our system (Table 1). In a typical organoid screening capture mode, our system can complete scanning in 42 s per well, or 3 min per plate, which is approximately a 2- to 5-fold improvement compared to the existing commercial system, despite the stage movement causing blurry images (data not shown).

Table 1 Evaluation of the speed of the "read-on-ski" system and two different commercial setups by whole-well scanning

Setup	Time (s)	Resolution (μm/pixel)
4× lens	42	1.55
10× lens	96	0.62
Cell Matric[1]	92	1.55
ImageXpress[2]	317	1.55

[1] Cell Matric DLC from Solentim Ltd. (UK); [2] ImageXpress Micro Confocal from Molecular Devices LLC (USA).

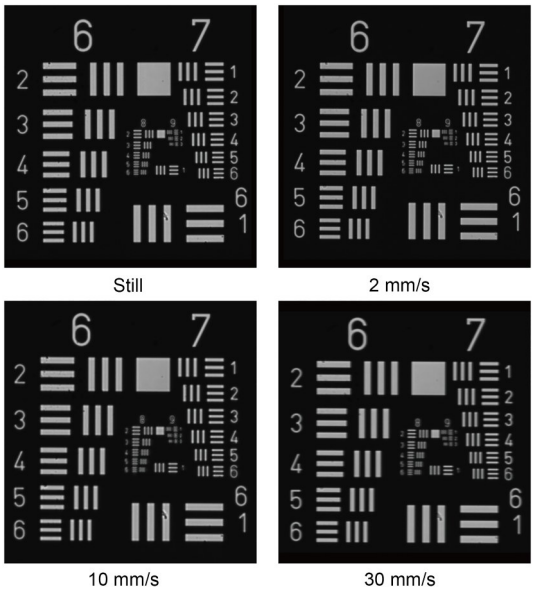

Fig. 4 Blur effect of the "read-on-ski" system at different running speeds.

3.2 Automated organoid detection using "read-on-ski" system

The "read-on-ski" system employed the optical stage movement with the static plate holding condition, which is ideal for suspension organoid screening. After whole-plate imaging, the morphological information of organoids, i.e., their differentiation and culturing status, was determined. We adopted a method that includes computational detection and recognition procedures. The strategy was to segment out the candidate organoids and automatically classify them into three categories (Figs. 5a–5i). Under high-quality imaging, well-developed organoids with structured tubule formation presented a unique texture, with various grayscale values under illumination compared to the background. Then, a threshold-based binarization was applied to distinguish the candidate area, which is based on the range of background intensity. The candidate area was filtered to retain the size between 200 and 1000 μm. Selected candidates were rescaled to 300 pixels×300 pixels and classified using a convolutional neural network (CNN) into three categories (Fig. 5j). We trained the CNN using over 1700 pre-labelled samples. Finally, the recognition results were mapped back to the entire well image, and the locations and labels were registered for the downstream process.

The recognition procedure for the kidney organoid detection framework consists of a two-stage classification process. If the image window is located in a positive organoid texture, the area is labelled using a green-colored overlay; the failed case is colored in blue, and the connected or adhesion organoids are

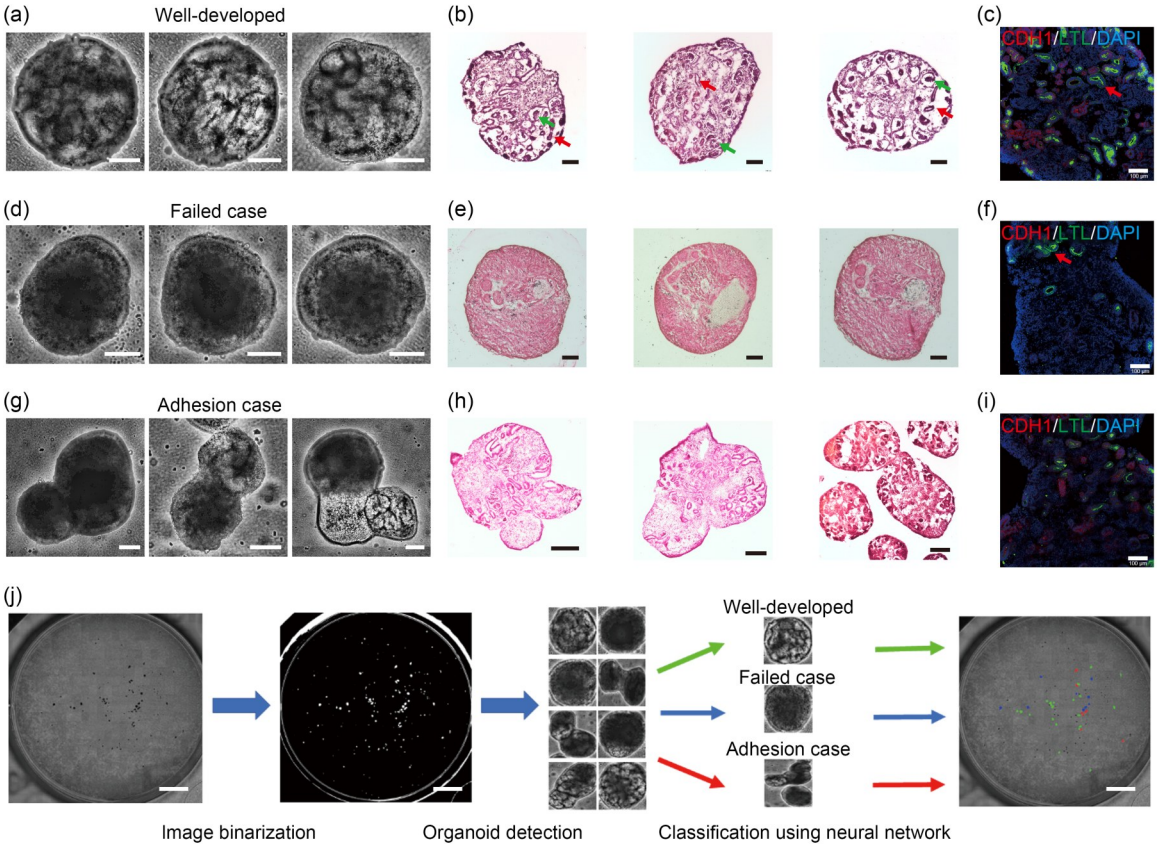

Fig. 5 Identification and classification of kidney organoids. (a–i) Characterization of well-developed, failed, and adhesion iPSC-derived 3D kidney organoids on Day 14: (a, d, g) Bright-field images of well-developed, failed, and adhesion kidney organoids, respectively; (b, e, h) H&E staining of well-developed, failed, and adhesion kidney organoid sections, respectively, with the red arrows indicating tubules and green arrows indicating podocytes; (c, f, i) Immunofluorescent staining of sections from well-developed, failed, and adhesion kidney organoids with proximal tubule marker LTL (green) and distal tubule marker CDH1 (red), and staining of nuclei with DAPI (blue), in which the red arrows indicate tubules. (j) Workflow of organoid detection using the "read-on-ski" system, with well-developed, failed, and adhesion kidney organoids being marked in green, blue, and red, respectively. iPSC: induced pluripotent stem cell; H&E: haematoxylin and eosin; LTL: lotus tetragonolobus lectin; CDH1: cadherin-1; DAPI: 4',6-diamidino-2-phenylindole. Scale bars: 100 μm (a–g, and i), 200 μm (h), and 5 mm (j).

marked in red and excluded (Fig. 5j). The training session was run with numerous manually cropped samples, followed by the annotation of the well-developed, failed, and adhesion groups, which were indicated at the regions after "read-on-ski" imaging and post-processing of an entire well plate. Subsequently, computer vision detection and categorization results were verified using conventional biomedical approaches. According to bright-field images (Figs. 5a, 5d, and 5g), the well-developed kidney organoids were verified using H&E staining, which showed more abundant components of tubules and podocytes than the failed cases (Figs. 5b and 5e). In contrast, H&E staining of adhesion kidney organoids indicated malformation of characteristic structures in the case of clumping (Fig. 5h). Immunostaining analysis of kidney organoid sections further consolidated and verified the computer vision detection results. LTL- and CDH1-positive staining demonstrated the formation of the proximal and distal tubules, which confirmed that immunostaining of well-developed kidney organoid sections consisted of label-free computer vision (Fig. 5c). The computer vision approach demonstrated 95% accuracy in the characterization of iPSC-derived 3D kidney organoids (Table 2).

3.3 Automated drug screening via organoid detection using the "read-on-ski" system

Current commercially available imaging setup methods cause blurry imaging due to system variations

Table 2 Accuracy rate of computer vision-assisted organoid detection

Classification of kidney organoids	Total number of cases	Correct case			Accuracy rate (%)
		Researcher A	Researcher B	Researcher C	
Well-developed	127	122	128	127	96.3±3.6
Failed case	203	201	192	191	95.9±2.7
Adhesion case	82	80	82	78	95.1±2.4

under the "stop-read" mode, which requires a prolonged phase for organoid settlement during image acquisition. Using the "read-on-ski" system to generate blur-free high-quality images via a label-free and non-invasive computer vision approach is expected to open avenues for organoid-based drug screening. To test this hypothesis, the kidney organoid-based toxicity model was used along with various concentrations of cisplatin and other similar compounds to mimic drug-induced renal damage (Fig. 6).

After induction, iPSCs were cultured for 14 d for differentiation into organoids. Continuous imaging was performed using the "read-on-ski" system to monitor the morphological characteristics of kidney organoids in multi-well culture plates (Figs. 6a–6c; before treatment). After image acquisition, the organoids in the multi-well plate were classified into three categories; in each well, the percentages of well-developed (positive, average organoids per well (81.9±2.4)%), failed (negative, average organoids per well (8.6±1.4)%), and adhesion case (multiple, average organoids per well (9.5±1.7)%) kidney organoids versus the overall detected events were calculated (Fig. 6d). Subsequently, the computer vision system digitally registered the organoids in classified categories and monitored them for cisplatin induction (0, 50, or 100 μmol/L) as an internal control for comparison purposes in toxicity screening. Following this strategy, organoids were imaged continuously for up to 96 h after cisplatin treatment. During this screening period, the computer vision system distinguished the changes in the organoid texture as tubule formation and changes in the organoid area as the change in size. The numbers of classified organoids before and after cisplatin treatment are summarized in Table S1. During the cisplatin toxicity study, the untreated control group showed minor changes in the negative category ((6.8±1.8)% vs. (15.6±7.2)%, not statistically significant) compared to a dramatic multi-fold increase in cisplatin-treated groups (50 μmol/L: (7.3±1.3)% vs. (30.5±2.6)%, P<0.05; 100 μmol/L: (8.0±3.0)% vs. (73.7±4.1)%, P<0.05). This observation demonstrated that the proportion of organoids in the negative category treated with 100 μmol/L cisplatin was significantly higher than that in the group treated with 50 μmol/L cisplatin ((73.7±4.1)% vs. (30.5±2.6)%, P<0.001), indicating dose-dependency (Fig. 6d). To verify the automated and algorithm-computed results, biological experiments were conducted using immunofluorescence staining and RT-qPCR analysis to verify cisplatin-treated or untreated control groups of organoid samples using a molecular approach. The fluorescence results indicated the protein expression level of the proximal tubule marker KIM1 (Figs. S5a–S5c). The messenger RNA (mRNA) levels of *KIM1* and proinflammatory cytokine gene *TNF-α* in 50 or 100 μmol/L cisplatin-treated organoids were significantly higher than those in the untreated control group (Fig. S5d). This finding was consistent with the results of the computer vision and algorithm-based detection methods. In contrast, including the untreated control group, the computer vision system showed that the proportion of positive organoids decreased under all conditions (control: (85.5±2.6)% vs. (40.6±7.5)%, P<0.01; 50 μmol/L: (86.4±3.2)% vs. (57.8±5.2)%, P<0.01; 100 μmol/L: (73.9±2.4)% vs. (4.7±2.6)%, P<0.001), as shown in Fig. 6d. The proportion of the adhesion category increased in the untreated control group ((7.7±2.1)% vs. (43.8±0.4)%, P<0.001) and in the higher dose of cisplatin group ((14.0±1.1)% vs. (30.1±3.6)%, P<0.05), whereas in the 50 μmol/L group, it remained unchanged ((6.4±3.3)% vs. (11.7±4.2)%, not statistically significant), as shown in Fig. 6d. Furthermore, an increase in the area of positive organoids as an indication of cellular proliferation also acted as a critical component to illustrate compound efficacy. The detected organoid area of positive cases significantly increased in the untreated control group ((0.144±0.007) mm^2 vs. (0.196±0.015) mm^2, P<0.001), whereas it decreased in the cisplatin-treated groups (50 μmol/L: (0.160±0.007) mm^2 vs. (0.095±0.005) mm^2, P<0.0001; 100 μmol/L: (0.160±0.008) mm^2 vs. (0.055±0.011) mm^2, P<0.0001), as shown in Fig. 6e. These data implied that organoids in the control group proliferated continuously

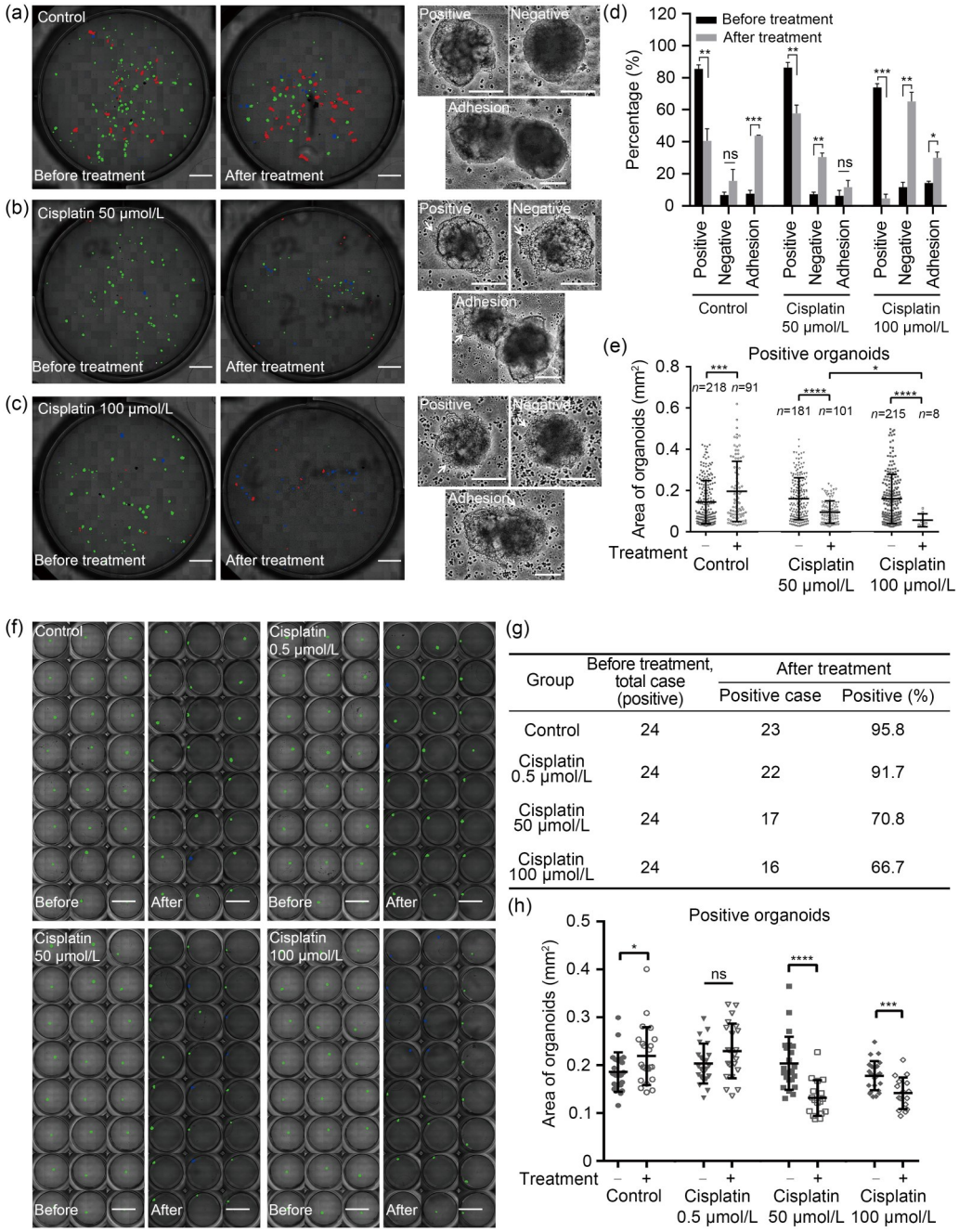

(g)

Group	Before treatment, total case (positive)	After treatment	
		Positive case	Positive (%)
Control	24	23	95.8
Cisplatin 0.5 μmol/L	24	22	91.7
Cisplatin 50 μmol/L	24	17	70.8
Cisplatin 100 μmol/L	24	16	66.7

Fig. 6 Cisplatin toxicity analysis using the "read-on-ski" system. (a–c) Organoids before and after treatment with cisplatin, detected using the "read-on-ski" system. Positive, negative, and adhesion kidney organoids are marked in green, blue, and red, respectively. Bright-field microscopy images showing positive, negative, and adhesion organoids after treatment with cisplatin. The white arrow shows the deteriorated organoid edge after treatment. (d) The percentages of positive, negative, and adhesion kidney organoids before and after treatment with cisplatin. (e) The area of positive organoids identified by the detection algorithm in different cisplatin-treated groups (control, 50 and 100 μmol/L). (f) Detection of organoids before and after treatment with cisplatin with indicated concentrations. Positive and negative cases of kidney organoids are marked in green and blue, respectively. Each cisplatin-treated group (0.5, 50, and 100 μmol/L) was placed in 96-well plates, with a single organoid per well. (g) A summary of cisplatin screening results of kidney organoids in 96-well plates. The detection algorithm calculated the proportions before and after treatment with different doses of cisplatin. (h) The area of positive organoids identified by the detection algorithm in different treatment conditions, as indicated in the data obtained from 96-well plate-based experiments. * $P<0.05$, ** $P<0.01$, *** $P<0.001$, **** $P<0.0001$, ^{ns} not significant. Scale bars: 200 μm (small figures in a–c) and 5 mm (big figures in a–c, and f).

as their size increased, which might have caused an increase in adhesive multi-organoid populations and indirectly reduced the number of positive organoids in culturing conditions (Figs. 6a and 6d). The computer vision approach showed results equivalent to those of serial imaging and endpoint measurement, which indicated cumulative renal damage caused by cisplatin (Figs. 6b and 6c).

The compound screening approach was implemented using the "read-on-ski" technology and an automated detection algorithm for drug screening in a 96-well plate format. One well per qualified well-developed organoid was handled as the screening setup. Each organoid was treated with cisplatin (0, 0.5, 50, or 100 μmol/L) and continuously imaged every 24 h via the "read-on-ski" approach for up to 96 h. The results showed that the percentage of positive organoids was reduced by the addition of cisplatin (Figs. 6f and 6g), and the average area alteration after cisplatin treatment was consistent with the results based on the multi-well plate (Fig. 6h). Moreover, the data were verified using multiple logistic regression analysis to determine the outcomes of cisplatin treatment. When the cisplatin concentration and the change in the detected area (delta area) were included in the multiple logistic regression model (Fig. S4), the positive-negative statement was predicted to be statistically significant in response to the changes in cisplatin concentration.

Furthermore, in order to demonstrate the imaging and detection, the combined setup is a generalized approach for pharmacological compound screening using kidney organoids (Fig. S6). The automated computer vision system provided a readout consistent with our previous half-maximal inhibitory concentration (IC_{50}) studies on celastrol and vitamin C, and matched the data obtained using conventional biological procedures to study kidney toxicity (data not shown).

4 Discussion

The application of kidney organoids in toxicity studies opens the door for future drug screening research. Conventional organoid toxicity studies rely on manual design, and the selection of features is based on human observation and experience, making it difficult to achieve optimal performance (Qian et al., 2016). The implementation of an automated stage-based microscopic setup for organoid screening has been limited by the spatial and temporal resolution of computational detection methods. Here, we have presented an automated label-free and non-invasive organoid-by-organoid screening setup, which employed our in-house developed "read-on-ski" system and machine learning-based computer vision algorithms. This setup can achieve 95% accuracy with three classifications of organoid status under a 3-min screening time with 1.2-μm spatial resolution on a standard multi-well plate (Table 2). Combining the automated image system with computer vision techniques can provide advanced tools for studies of biological morphology and classification in organoid-based toxicity trials (Schmuck et al., 2017).

The application of organoids has shown great potential for drug screening (Boretto et al., 2019; Driehuis et al., 2020), but it has not been utilized by the pharmaceutical industry or commercialized for related research outside the academic environment. As reported here, in conjunction with automated imaging ability, a computer-aided machine learning approach for organoid-based drug screening can detect cellular changes in the early stages and quantitatively extract multi-parameter features (Fig. 5j). Image quality is key to this computer-assisted approach. Unlike the conventional setup, the optical setup developed here can hold 3 μm of the depth of field with a 0.4 numerical aperture, which is sufficient to capture an area of 1.4 mm× 1.6 mm (Fig. 4). The imaging process can capture the entire 96-well plate with a generous depth of field; hence, tubule formation in kidney organoids classified with different features and sizes can be registered. As the time lapse is elevated at high frequency, this automated high-throughput analysis can potentially group different stages as individual conditions for kidney organoid changes in cell fate mapping.

Computer-assisted cell recognition has been widely used in life science research. Big data are used to directly train multi-layer neural networks with different deep structures and to combine these networks with feature extraction and classification. A CNN is a structure introduced by LeCun and Bengio (1995), which is widely used in computer vision research. CNNs are successfully applied to manage image data in classification, segmentation detection, and retrieval tasks. For example, CNNs are used as the current

baseline approach for breast cancer classification and diagnosis (Chougrad et al., 2018). Chen et al. (2016) presented a multi-feature, label-free cell classification system using deep learning techniques. Deep learning techniques provide an end-to-end learning procedure that combines feature extraction with a classifier. The expert pre-labelled samples provide a limited training set, which cannot completely cover all types and phenotypes. Thus, increasing the number and diversity of samples to enhance the training set may further improve the accuracy. However, in this study, we could not form a correlation between failed cases with false positives or negatives logically; the detection failure was commonly unknown owing to the characterization of the CNN itself.

The entire well plate was imaged to detect different unveiled organoid alterations during cisplatin treatment. This single organoid detection approach revealed that over 96 h, the organoids continued to grow, and we could not use a single parameter to describe the efficacy of the treatment, although various concentrations were used (Fig. 6d). The loss of the tubule structure (reduction in positive and increase in negative cases) and reduced sizes can be the generalized key signatures for toxicity studies (Figs. 6d and 6e). Overgrown organoids formed adhesion sets in multiple organoids; a similar observation was obtained in profoundly demanded kidney organoids. Although the observations and quantification methods indicated a similar effect, the mechanisms of merging of the organoids were different.

The application of fully automated imaging-based organoid screening in toxicity studies will open the door for next generation drug screening (Fig. 7). The texture-related multicellular formation of the structural features and the changes in the size of the organoids are fundamental criteria to be considered under the same conditions.

Acknowledgments

This research was funded by the Scientific Instrumentation Development Program of Chinese Academy of Sciences (No. ZDZBGCH2018005), the Key Research and

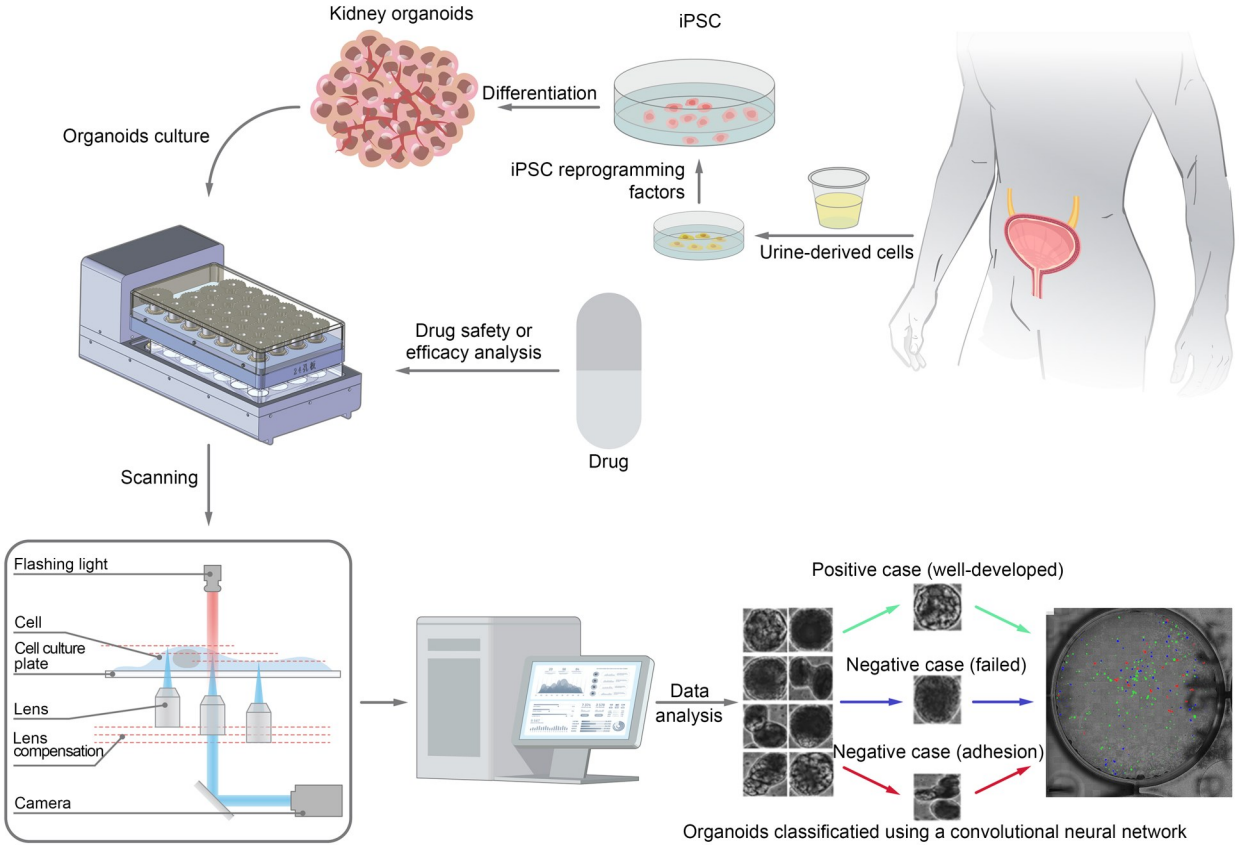

Fig. 7 "Read-on-ski" automated imaging and label-free detection system for toxicity screening using personalized human kidney organoids. iPSC: induced pluripotent stem cell.

Development Program of Bioland Laboratory (Guangzhou Regenerative Medicine and Health Guangdong Laboratory) (No. 2019GZR1104060), and the Research Instrument and Equipment Development Project of Chinese Academy of Sciences (No. ZDKYYQ20210006), China.

Author contributions

Meijin GUO and Xiao ZHANG initiated this study and coordinated the project. Qizheng WANG, Jun LU, Ke FAN, Yiwei XU, and Yucui XIONG performed the experimental research. Zhiyong SUN, Man ZHAI, Zhizhong ZHANG, Sheng ZHANG, Yan SONG, and Jianzhong LUO performed the data analysis. Mingliang YOU and Meijin GUO contributed to review. Xiao ZHANG, Qizheng WANG, and Yiwei XU contributed to the study design, data analysis, writing and editing of the manuscript. All authors have read and approved the final manuscript, and therefore, have full access to all the data in the study and take responsibility for the integrity and security of the data.

Compliance with ethics guidelines

Qizheng WANG, Jun LU, Ke FAN, Yiwei XU, Yucui XIONG, Zhiyong SUN, Man ZHAI, Zhizhong ZHANG, Sheng ZHANG, Yan SONG, Jianzhong LUO, Mingliang YOU, Meijin GUO, and Xiao ZHANG declare that they have no conflict of interest.

All experiments were performed according to the guidelines set by the Human Subject Research Ethics Committee at Guangzhou Institutes of Biomedicine and Health (GIBH) and the Chinese Academy of Sciences (CAS), and the Committee approved the experiments (approval number: GIBH-IRB07-2017039).

References

Boretto M, Maenhoudt N, Luo XL, et al., 2019. Patient-derived organoids from endometrial disease capture clinical heterogeneity and are amenable to drug screening. *Nat Cell Biol*, 21(8):1041-1051. https://doi.org/10.1038/s41556-019-0360-z

Bracewell RN, 1986. The Fourier Transform and its Applications. McGraw-hill, New York, USA.

Carpenter MK, Frey-Vasconcells J, Rao MS, 2009. Developing safe therapies from human pluripotent stem cells. *Nat Biotechnol*, 27(7):606-613. https://doi.org/10.1038/nbt0709-606

Chen CL, Mahjoubfar A, Tai LC, et al., 2016. Deep learning in label-free cell classification. *Sci Rep*, 6:21471. https://doi.org/10.1038/srep21471

Chougrad H, Zouaki H, Alheyane O, 2018. Deep convolutional neural networks for breast cancer screening. *Comput Methods Programs Biomed*, 157:19-30. https://doi.org/10.1016/j.cmpb.2018.01.011

Ciampi O, Iacone R, Longaretti L, et al., 2016. Generation of functional podocytes from human induced pluripotent stem cells. *Stem Cell Res*, 17(1):130-139. https://doi.org/10.1016/j.scr.2016.06.001

Davies JA, 2015. Biological techniques: kidney tissue grown from induced stem cells. *Nature*, 526(7574):512-513. https://doi.org/10.1038/nature15639

Digby JLM, Vanichapol T, Przepiorski A, et al., 2020. Evaluation of cisplatin-induced injury in human kidney organoids. *Am J Physiol Renal Physiol*, 318(4):F971-F978. https://doi.org/10.1152/ajprenal.00597.2019

Driehuis E, Kretzschmar K, Clevers H, 2020. Establishment of patient-derived cancer organoids for drug-screening applications. *Nat Protoc*, 15(10):3380-3409. https://doi.org/10.1038/s41596-020-0379-4

Ebert AD, Yu JY, Rose FF, et al., 2009. Induced pluripotent stem cells from a spinal muscular atrophy patient. *Nature*, 457(7227):277-280. https://doi.org/10.1038/nature07677

Fan K, Zhang S, Zhang Y, et al., 2017. A machine learning assisted, label-free, non-invasive approach for somatic reprogramming in induced pluripotent stem cell colony formation detection and prediction. *Sci Rep*, 7:13496. https://doi.org/10.1038/s41598-017-13680-x

Hinchcliffe EH, 2005. Using long-term time-lapse imaging of mammalian cell cycle progression for laboratory instruction and analysis. *Cell Biol Educ*, 4(4):284-290. https://doi.org/10.1187/cbe.05-02-0064

Hosmer DW, Lemesbow S, 1980. Goodness of fit tests for the multiple logistic regression model. *Commun Stat Theory Methods*, 9(10):1043-1069. https://doi.org/10.1080/03610928008827941

Ichimura H, Shiba Y, 2017. Recent progress using pluripotent stem cells for cardiac regenerative therapy. *Circ J*, 81(7):929-935. https://doi.org/10.1253/circj.CJ-17-0400

Imig JD, Ryan MJ, 2013. Immune and inflammatory role in renal disease. *Compr Physiol*, 3(2):957-976. https://doi.org/10.1002/cphy.c120028

Jansen J, Schophuizen CMS, Wilmer MJ, et al., 2014. A morphological and functional comparison of proximal tubule cell lines established from human urine and kidney tissue. *Exp Cell Res*, 323(1):87-99. https://doi.org/10.1016/j.yexcr.2014.02.011

Jones SA, Shim SH, He J, et al., 2011. Fast, three-dimensional super-resolution imaging of live cells. *Nat Methods*, 8(6):499-505. https://doi.org/10.1038/nmeth.1605

Koning M, van den Berg CW, Rabelink TJ, 2020. Stem cell-derived kidney organoids: engineering the vasculature. *Cell Mol Life Sci*, 77(12):2257-2273. https://doi.org/10.1007/s00018-019-03401-0

Krizhevsky A, Sutskever I, Hinton GE, 2012. ImageNet classification with deep convolutional neural networks. Proceedings of the 25th International Conference on Neural Information Processing Systems, Lake Tahoe, p.1097-1105.

LeCun Y, Bengio Y, 1995. Convolutional networks for images, speech, and time-series. *In*: Arbib MA (Ed.), The Handbook of Brain Theory and Neural Networks. MIT Press, Cambridge, p.1995.

Liyanage T, Ninomiya T, Jha V, et al., 2015. Worldwide access to treatment for end-stage kidney disease: a systematic review. *Lancet*, 385(9981):1975-1982. https://doi.org/10.1016/s0140-6736(14)61601-9

Lu J, Fan WH, Huang ZH, et al., 2022. Automatic system for high-throughput and high-sensitivity diagnosis of SARS-CoV-2. *Bioprocess Biosyst Eng*, 45(3):503-514. https://doi.org/10.1007/s00449-021-02674-9

Przepiorski A, Sander V, Tran T, et al., 2018. A simple bioreactor-based method to generate kidney organoids from pluripotent stem cells. *Stem Cell Reports*, 11(2):470-484. https://doi.org/10.1016/j.stemcr.2018.06.018

Qian XY, Nguyen HN, Song MM, et al., 2016. Brain-region-specific organoids using mini-bioreactors for modeling ZIKV exposure. *Cell*, 165(5):1238-1254. https://doi.org/10.1016/j.cell.2016.04.032

Ronneberger O, Fischer P, Brox T, 2015. U-Net: convolutional networks for biomedical image segmentation. International Conference on Medical Image Computing and Computer-Assisted Intervention. Springer, Cham, p.234-241. https://doi.org/10.1007/978-3-319-24574-4_28

Schmuck MR, Temme T, Dach K, et al., 2017. Omnisphero: a high-content image analysis (HCA) approach for phenotypic developmental neurotoxicity (DNT) screenings of organoid neurosphere cultures in vitro. *Arch Toxicol*, 91(4):2017-2028. https://doi.org/10.1007/s00204-016-1852-2

Shi YH, Inoue H, Wu JC, et al., 2017. Induced pluripotent stem cell technology: a decade of progress. *Nat Rev Drug Discov*, 16(2):115-130. https://doi.org/10.1038/nrd.2016.245

Sirenko O, Mitlo T, Hesley J, et al., 2015. High-content assays for characterizing the viability and morphology of 3D cancer spheroid cultures. *Assay Drug Dev Technol*, 13(7):402-414. https://doi.org/10.1089/adt.2015.655

Stephens DJ, Allan VJ, 2003. Light microscopy techniques for live cell imaging. *Science*, 300(5616):82-86. https://doi.org/10.1126/science.1082160

Su R, Xiong SJ, Zink D, et al., 2016. High-throughput imaging-based nephrotoxicity prediction for xenobiotics with diverse chemical structures. *Arch Toxicol*, 90(11):2793-2808. https://doi.org/10.1007/s00204-015-1638-y

Sun W, Zhang S, Zhou TC, et al., 2020. Human urinal cell reprogramming: synthetic 3D peptide hydrogels enhance induced pluripotent stem cell population homogeneity. *ACS Biomater Sci Eng*, 6(11):6263-6275. https://doi.org/10.1021/acsbiomaterials.0c00667

Tasnim F, Deng RS, Hu M, et al., 2010. Achievements and challenges in bioartificial kidney development. *Fibrogenesis Tissue Repair*, 3:14. https://doi.org/10.1186/1755-1536-3-14

Tiong HY, Huang P, Xiong SJ, et al., 2014. Drug-induced nephrotoxicity: clinical impact and preclinical *in vitro* models. *Mol Pharm*, 11(7):1933-1948. https://doi.org/10.1021/mp400720w

Wang QZ, Xiong YC, Zhang S, et al., 2021. The dynamics of metabolic characterization in iPSC-derived kidney organoid differentiation *via* a comparative omics approach. *Front Genet*, 12:632810. https://doi.org/10.3389/fgene.2021.632810

Wijnen B, Petersen EE, Hunt EJ, et al., 2016. Free and open-source automated 3-D microscope. *J Microsc*, 264(2):238-246. https://doi.org/10.1111/jmi.12433

Zuiderveld K, 1994. VIII.5.—Contrast limited adaptive histogram equalization. *In*: Heckbert PS (Ed.), Graphics Gems IV. Academic Press, Boston, p.474-485. https://doi.org/10.1016/B978-0-12-336156-1.50061-6

Supplementary information

Table S1; Figs. S1–S6